



American Institute of Aeronautics and Astronautics

AIAA 2002-0218

Aeroheating Predictions for the X-43 Cowl-Closed Configuration at Mach 7 and 10

Charles E. Cockrell, Jr.
Aaron H. Auslender
Jeffrey A. White
NASA Langley Research Center
Hampton, Virginia

Arthur D. Dilley
Raytheon, Inc.
Tucson, Arizona

**40th AIAA Aerospace Sciences Conference & Exhibit
14-17 January 2002 / Reno, Nevada**

Aeroheating Predictions for the X-43 Hyper-X Cowl-Closed Configuration at Mach 7 and 10

Charles E. Cockrell, Jr.^{*}, Aaron H. Auslender[†] and Jeffrey A. White[‡]
NASA Langley Research Center, Hampton, VA
And
Arthur D. Dilley[§]
Raytheon, Inc., Tuscon, AZ

Abstract

A pre-flight analysis was conducted for the Mach 7 and Mach 10 X-43 cowl-closed configurations to evaluate three-dimensional flow-field effects on localized heating in the vicinity of the closed cowl flap and sidewall. First, engineering-level analyses based on documented laminar and turbulent surface heating database were used to estimate localized heating amplification factors to account for turbulent flow effects, corner flow effects and the presence of forebody boundary layer trip devices. These estimated factors were applied to 2-D computational predictions to develop surface heat loads. Second, thin-film gauge surface heating data were obtained for a Mach 10 cowl-closed configuration in a reflected shock tunnel at simulated flight conditions. Third, computational fluid dynamics (CFD) flow-field predictions were obtained at Mach 10 ground-test conditions to provide comparisons with the engineering database predictions and experimental measurements. Similarly, a CFD solution was also obtained at Mach 7 flight conditions to provide qualitative comparisons with engineering predictions. The Mach 10 CFD predictions compare favorably with the experimental measurements and the engineering estimates for surface heating amplification on the closed cowl. However, experimental measurements were not of sufficient quantity on the sidewall surface to

capture the highest localized heating rates, and also the Mach 10 CFD predictions suggest higher peak heating on the sidewall compared to the engineering estimates. Also, the Mach 7 CFD predictions indicate qualitative agreement with the database estimates in terms of flow-field structure and peak heating locations on the closed-cowl flap and sidewall surfaces.

Nomenclature

C_p	Pitot Pressure Coefficient, $\frac{p_t - p_\infty}{q_\infty}$
p_t	Pitot Pressure (psi)
p_∞	Freestream static pressure (psi)
q	Surface heat flux, Btu/(ft ² sec)
q_∞	Freestream dynamic pressure (psi)
x, y, z	Model Coordinates, inches
y^+	Grid spacing parameter
Δy	Distance from surface to first cell center, inches
μ	Viscosity coefficient, lbf-sec/ft ²
ρ_w	Density at the wall, slugs/ft ³
τ_w	Shear stress at the wall, lbf/ft ²

Introduction

The National Aeronautics and Space Administration (NASA) has established goals for third-generation space transportation systems to reduce the cost and improve the reliability of delivering payloads to orbit. An ambitious technology development program is underway to mature design and analysis tools and validate the performance of candidate airbreathing and combined-cycle engine and vehicle concepts in relevant ground and flight environments. This paper addresses a key design and analysis methodology to predict three-dimensional flow-field effects on the surface heating. Engineering database predictions, experimental data and computational fluid dynamics (CFD) predictions are presented at Mach 10 conditions. Engineering database and CFD predictions are presented at Mach 7 conditions.

^{*} Airbreathing Propulsion Technology Manager, Hypersonic Airbreathing Propulsion Branch, Senior Member, AIAA.

[†] Assistant Head, Hypersonic Airbreathing Propulsion Branch.

[‡] Aerospace Engineer, Hypersonic Airbreathing Propulsion Branch.

[§] Senior Systems Engineer, Aeromechanics Design Department.

Copyright © 2002 by American Institute of Aeronautics and Astronautics, Inc. No copyright is asserted in the United States under Title 17, U.S. Code. The U.S. Government has a royalty-free license to exercise all rights under the copyright claimed herein for governmental purposes. All other rights are reserved by the copyright owner.

The X-43, or Hyper-X, program was initiated to demonstrate the performance of hydrogen-fueled, airframe-integrated, scramjet propulsion systems in flight and to obtain performance data to validate design tools and analysis methods. Details of the program are included in reference 1. The first Mach 7 flight attempt resulted in a failure of the booster rocket to deliver the X-43 research vehicle to the scramjet flight test condition. An additional Mach 7 flight and a Mach 10 flight are planned. A sketch of the X-43 research vehicle is shown in Figure 1.

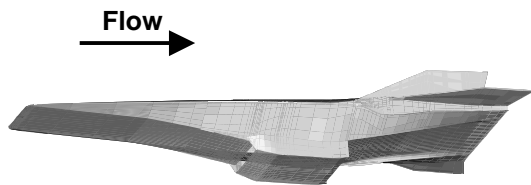


Figure 1. X-43 Hyper-X Research Vehicle.

The X-43 research vehicle is boosted to the flight test altitude by the first stage of a Pegasus[®] booster rocket. The Hyper-X Launch Vehicle (HXLV) refers to the configuration with the research vehicle attached to the booster. During the boost phase of the mission and immediately following separation of the X-43 vehicle, a cowl flap is used to close off the engine flowpath and divert the forebody flow around the external cowl. The cowl flap is actuated to the open position as the vehicle reaches the flight test condition prior to the scramjet test phase of the mission. A sketch of the cowl-closed configuration near the cowl leading edge is shown in Figure 2. Although the cowl is in the closed position, a small gap exists between the cowl leading edge and the forebody surface, allowing some flow to be entrained into the internal flowpath. Also, boundary-layer trip mechanisms have been placed on the forebody surface upstream of the first compression ramp break in order to ensure that turbulent flow enters the inlet.

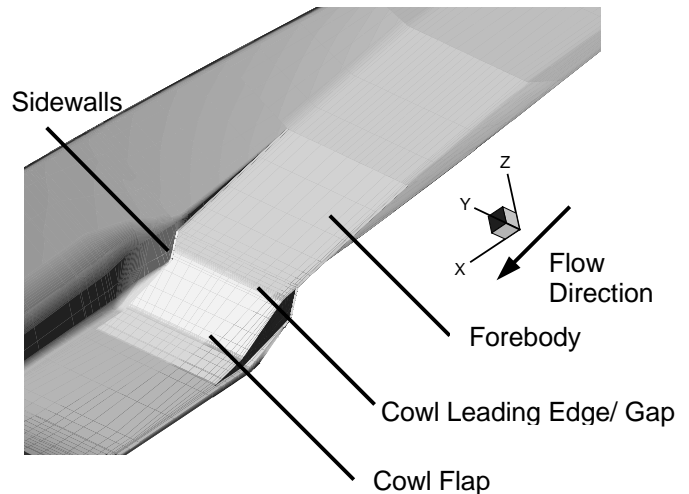


Figure 2. X-43 closed-cowl configuration.

Prior to these flights, an extensive ground testing and analysis program was conducted to investigate various aspects of vehicle performance, validate design tools and provide risk reduction for the flight experiments. Among the areas studied were scramjet flowpath performance, aero-propulsive vehicle performance and aero-thermal loads definition for the vehicle and engine flowpath.

A significant pre-flight development effort was devoted to predicting surface heating for the vehicle and engine flowpath. In particular, an accurate definition of aero-thermal loads on the closed cowl and sidewall surfaces was necessary to ensure material survivability during ascent and to eliminate the potential of binding between the cowl flap and sidewall surfaces, which could prevent the flap from actuating properly following vehicle separation prior to the scramjet test point. Three-dimensional flow-field effects, such as corner and shock-boundary layer interactions have a significant impact on surface heating. Additionally, the shocks generated from the cowl leading edge sweep across the inboard side of the sidewall surface and produce localized heating amplification.

A multi-level analysis approach was used to account for these effects in the pre-flight thermal analysis. Initial predictions for aerothermodynamic heating on X-43 airframe surfaces were obtained from two-dimensional CFD solutions. The 2-D CFD heating predictions were augmented for both Mach 7 and Mach 10 flight conditions using engineering database

estimates based on documented laminar and turbulent heating data, and data from a series of Hyper-X boundary layer trip device tests. The engineering-level analysis indicates that there is sufficient thermal design margin at the Mach 7 flight condition for hardware survivability. However, the Mach 10 heating may impact the amount of coolant required during boost and the scramjet test portion of the flight.

Experimental surface heating data were obtained for both the cowl-closed and cowl-open configurations at simulated Mach 10 flight conditions. These data are used to provide comparisons with the engineering database estimates to evaluate relative surface heating amplification rates on the cowl-flap and sidewall surfaces. Finally, Navier-Stokes CFD calculations were obtained at Mach 10 wind-tunnel conditions to provide comparisons with, and interpretation of, the experimental measurements and to provide a qualitative assessment of flow-field features that contribute to peak localized surface heating on the cowl flap and sidewalls. A 3-D calculation was also obtained at Mach 7 flight conditions to qualitatively assess flow-field features and their impact on localized surface heating.

Engineering Analysis

Documented experimental databases were used to develop engineering-level estimates in the form of surface heating amplification factors to account for enhanced localized heating to augment the initial two-dimensional CFD predictions. Enhanced heating in the localized regions is produced by residual forebody trip-induced boundary layer/vortex interactions with the closed cowl, turbulent flow effects on the sidewall surfaces, shock-boundary layer interactions and end-effect heating on the cowl flap surface, and sidewall heating from corner flow effects.

The engineering database estimates were developed using existing experimental databases consisting of laminar and turbulent heating from shock/boundary layer interactions^{2,3} and experimental results used to evaluate the effectiveness of the X-43 boundary-layer trip devices.⁴ These existing data were based on lower Mach number data sets and were extrapolated to the Mach 7 and Mach 10 conditions. The database estimates predicted a heating augmentation factor of 20-percent on

the cowl flap to account for enhanced heating because of vortex impingement generated by the forebody boundary-layer trips at both Mach 7 and Mach 10. In order to account for corner effects, a linearly varying amplification factor was applied in a region extending from 5-percent to 15-percent of the cowl-flap width, starting in the corner. The maximum heating amplification factor of twice the center-line turbulent value was applied in a region extending 5-percent of the flap width from the corner.

The effect of the cowl leading edge shock waves sweeping across the inboard side of the sidewall surfaces was captured by applying heating amplification factors to two-dimensional laminar flat-plate calculations. The assessment of the increase in heating from laminar flat plate values to a maximum amplification value was based on the localized maximum laminar heating data presented by Hackett.³ This maximum heating amplification factor is approximately 15 times the undisturbed laminar freestream value, specific to the Mach 7 and Mach 10 conditions.

Mach 10 Cowl-Closed Ground Tests

Experimental tests were conducted to obtain surface heating and pressure data for the cowl-closed configuration at nominal Mach 10 flight conditions. The tests were conducted in Leg 1 of the Large Energy National Shock (LENS) hypervelocity tunnel located at Calspan-University of Buffalo Research Center (CUBRC). This facility is a reflected shock tunnel with an electrically heated driver section capable of duplicating flight total enthalpy conditions up to a Mach number of 12. The capabilities of this facility are described in reference 5.

Figure 3 shows the Mach 10 scramjet engine configuration tested in the LENS facility. The test article consists of a two-dimensional forebody plate, used to duplicate the forebody compression conditions of the Mach 10 X-43 vehicle. The cowl-closed configuration, shown in figure 4, models the Mach 10 X-43 vehicle outer mold line in the vicinity of the cowl flap and sidewalls. The model was tested with and without the flight-like boundary-layer trip devices. Thin-film heat transfer gauges and pressure taps are located on the forebody boundary-layer plate, cowl flap and sidewall surfaces. Also, figure 4 shows the surface

instrumentation on the cowl flap and sidewall surfaces.

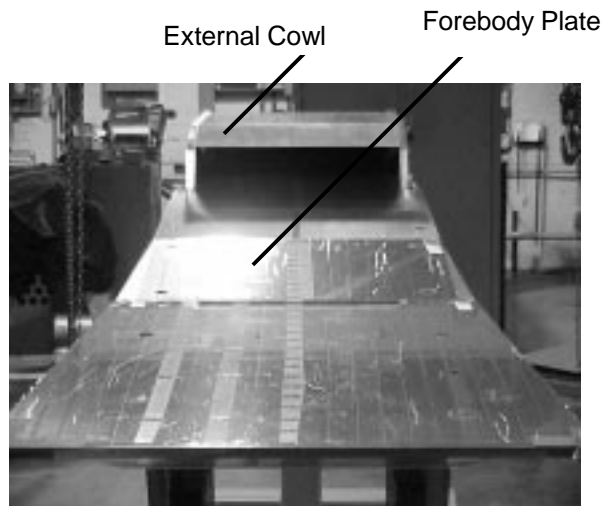


Figure 3. Photograph of Mach 10 X-43 scramjet test model at CUBRC.

Thin-film gauges on surfaces

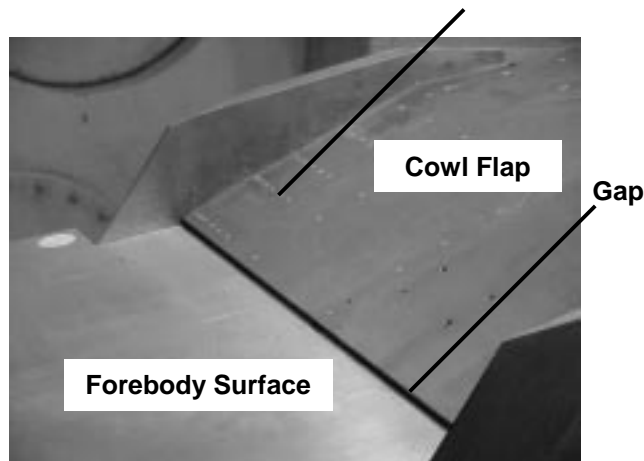


Figure 4. Mach 10 cowl-closed configuration with sidewall and cowl flap instrumentation.

Data from two of the cowl-closed experimental runs are presented in the paper. Both runs are at the nominal Mach 10 simulated flight conditions (see Table 1) and correspond to a 1° angle-of-attack orientation. Run-6 data were obtained with the boundary-layer trip devices mounted on the forebody surface and Run-4 data were obtained without trips. Primarily, results from Run 6 are used to provide comparisons with computations. The Run-4

results are used to illustrate differences in surface heating because of the boundary-layer trips. Table 1 presents a summary of both Run-4 and Run-6 flow conditions as indicated in the test data report. Table 2 shows the major species constituents of the test-gas composition.

Table 1. Freestream Conditions for Mach 10 cowl-closed runs.

Parameter	Run 6	Run 4
Mach	10.7	10.5
Static Temp (deg. R)	368	391
Static Pressure (psi)	0.092	0.11

Table 2. Test-gas composition.

Species	Mass Fraction
N ₂	0.749
O ₂	0.178
Ar	0.009
NO	0.064
γ	1.401

CFD Solution Methodology

CFD solutions were obtained at the Mach 10 wind-tunnel and Mach 7 flight conditions to examine the flow-field structure, localized heating areas, and aerothermodynamic heating in the vicinity of the cowl leading edge in the closed position. Solutions were obtained using the Viscous Upwind Algorithm for Complex Flow Analysis (VULCAN). VULCAN is a three-dimensional, cell-centered, structured-grid, Navier-Stokes flow solver that includes message-passing interface (MPI) capability to solve multi-block topologies utilizing distributed-memory parallel architectures.⁶

Mach 10 Solution Procedure

The surface geometry used for the Mach 10 solution modeled the CUBRC test configuration. CFD was performed using the flow conditions of Run 6, as listed in tables 1 and 2. A solution of the forebody plate was produced using the two-dimensional parabolized Navier-Stokes (PNS) option of VULCAN. (The forebody leading edge was solved as an elliptic region to initialize the solution.) This procedure assumes uniform flow conditions in the facility test section and neglects the effects of flow

spillage around the sides of the forebody plate. The boundary layer was modeled as laminar from the leading edge until the first compression ramp break, and then fully turbulent downstream of this station using the Wilcox $k-\omega$ turbulence model.⁷ This procedure is consistent with previous computational modeling of the X-43⁸ as well as with experimental data which indicate the effectiveness of the flight-like trip devices.⁹ Note, however, that the boundary-layer trips were not modeled in the calculations. In addition, a no-slip, isothermal, cold-wall boundary condition was used with a fixed wall temperature of 531.8 °R. The cold-wall boundary condition is valid because test times in the LENS facility do not allow for significant model heating during a run.

After convergence, the 2-D forebody-plate solution was projected onto a three-dimensional computational grid as an inflow boundary condition and as an initial condition for the 3-D fully elliptic solution of the cowl flap and sidewall region. The surface grid incorporates the cowl-flap and sidewall regions of the Mach 10 X-43 cowl-closed configuration and includes the gap between the forebody and cowl leading edge, the blunt cowl and sidewall leading edges. The 3-D elliptic region utilized a multi-block grid topology consisting of 48 blocks and was solved using 16 processors with approximately 0.9-0.95 million grid points per processor. Non-continuous grid-point interfaces were used at the block boundary interfaces, which decreased the total grid size. Fine grid density is required to resolve the blunt cowl and sidewall leading edges and to provide sufficient grid resolution to model three-dimensional flow effects and surface heat transfer rates. After obtaining the elliptic corner-flow solution, the region downstream of external cowl flap was solved using the PNS marching algorithm, with the matching portion of the elliptic region as a boundary condition.

Mach 7 Solution Procedure

Similar to the Mach 10 solution, a three-dimensional flow-field prediction was obtained for a portion of the Mach 7 X-43 cowl-closed configuration, including the nose, forebody, cowl flap and sidewalls. The downstream portion of the external cowl and aftbody portions of the configuration were not solved since the purpose of this study was to examine the heating rates on the cowl flap and inboard sidewall surfaces. Unlike the Mach 10 solution, which was obtained

at wind-tunnel conditions, the Mach 7 solution was obtained at a flight condition of Mach 7.3 and -1.4° angle-of-attack, corresponding to conditions of the baseline Mach 7 trajectory where the maximum aerodynamic heating occurs.

A multi-block grid topology, consisting of both elliptic and space-marching zones, was used in the calculation to capture the physics in the regions of interest. The nose was solved using a full Navier-Stokes (elliptic) procedure and the forebody was solved using a PNS (space marching) procedure. The elliptic solver was employed to solve the flow field near the cowl leading edge, including the surface gap, the blunt sidewall and the cowl leading edge. Subsequent to converging the elliptic calculation, the marching solution was continued along the cowl flap. Figure 5 shows the Mach 7 grid topology.

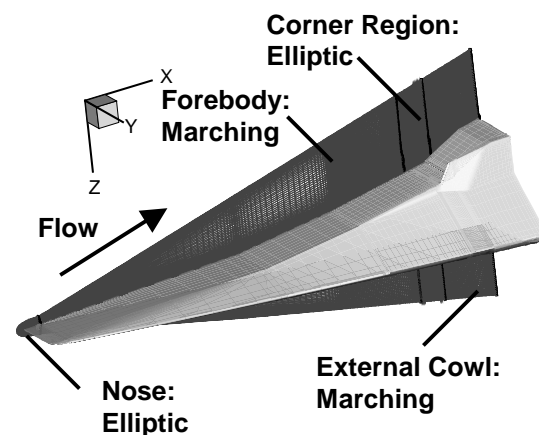


Figure 5. Mach 7 3-D Grid Topology and solution technique.

The elliptic nose solution utilized 6 processors with approximately 500,000 grid points per processor. The elliptic cowl/sidewall region utilized 11 processors with approximately 1.7-1.75 million grid points per processor, distributed among 61 blocks. The forebody marching region has a total of 15 million grid points distributed among 41 blocks and the marching cowl flap region has a total of 3.5 million grid points. The marching regions were solved using 6 processors.

Similar to the Mach 10 solution methodology, the nose and forebody regions were modeled with laminar boundary layers until the first compression corner and then with a fully

turbulent boundary layer aft of this station to simulate the effects of the boundary-layer trips. Solid surfaces were modeled with a no-slip, isothermal wall boundary condition with a fixed wall temperature of 1000° R. This methodology is consistent with previous computational modeling of the X-43 configuration at the Mach 7 flight conditions⁸ and with the methodology used to size the flight boundary-layer trip configurations to provide transition onset prior to the end of the first ramp.⁹

Results and Discussion

Mach 10 Condition

The Mach 10 results are presented by first showing comparisons between the 2-D forebody calculation and experimental data followed by surface heating comparisons on the cowl flap and sidewall surfaces. Also, qualitative comparisons with the engineering- database predictions are discussed.

Figure 6 shows a plot of predicted pitot pressure coefficient values from the Mach 10 2-D forebody plate calculation compared with experimental pitot rake data obtained from the Mach 10 CUBRC tests. Figure 7 shows a photograph of the pitot pressure rake installed with the cowl-closed model. The predicted peak pitot pressure values compare well with the data obtained for the run without the boundary-layer trip devices near the wall. Thus, the near-wall grid density is sufficient to match the experimental data. However, the measured peak

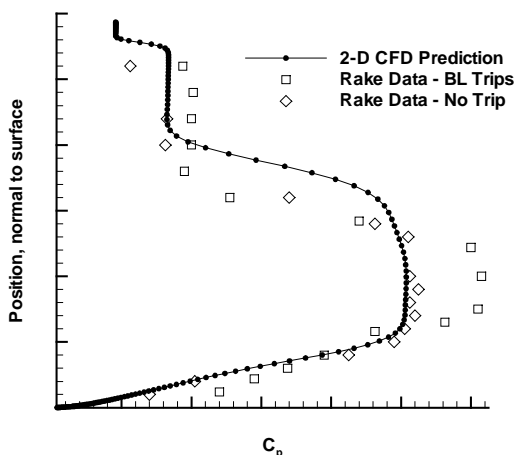


Figure 6. Comparison of predicted and measured pitot pressure values at Mach 10.

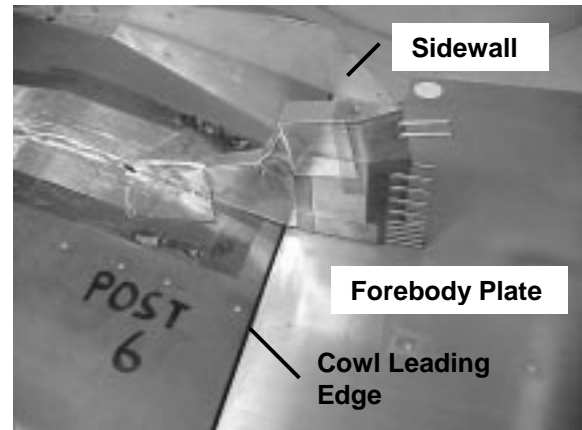


Figure 7. Photograph of boundary-layer rake mounted on cowl-closed configuration.

values are higher for the trip configuration. Generally, pitot pressure values away from the body surface compare favorably between predictions and measurements. Although there is reasonable qualitative agreement between the predictions and data, some discrepancy is observed between measured and predicted shock locations. This discrepancy may be caused by test section flow condition variations and 3-D edge effects of the forebody plate, which were not modeled in the 2-D calculation. The data also indicate that the boundary-layer trips have a localized effect on pitot-pressure values because of shock/vortex interactions. However, the flow structure further away from the body surface does not appear to be significantly affected.

Figure 8 shows surface heating comparisons between the 2-D forebody-plate predictions and surface heating measurements. The heating rates were non-dimensionalized by the measured and predicted values at a location 3-inches aft of the nose, which is where the first thin-film gauge is located on the forebody plate. Data are shown for both the trip and no-trip configurations. The CFD predictions are generally bounded by these two sets of measurements downstream of the $x=38$ -inch station. Considering assumptions made in modeling the tunnel conditions and the forebody plate geometry, the predictions show reasonable qualitative agreement with the no-trip data upstream of the first compression ramp break, where the solution is modeled as laminar. The experimental trip data indicate an increase in surface heating because of a combination of the turbulent boundary layer and interaction

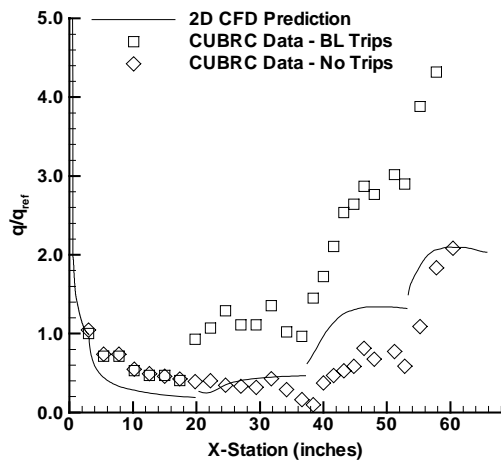


Figure 8. Comparison of predicted and measured forebody heating rates at Mach 10.

between residual trip-induced vortices and boundary layers on the forebody surface. The engineering database indicated a 20-percent amplification factor to account for such interaction effects on the cowl flap surface.

Figure 9 shows Mach number contours at the symmetry plane of the calculation in the region of the cowl flap. This figure highlights the gap between the cowl leading edge and the forebody surface. The cowl leading edge is enveloped in the fully turbulent boundary layer generated along the forebody surface, but still processes supersonic flow. Also, note that the generated bow shock interacts with the forebody boundary layer to produce a separation region inside the gap.

Figure 10 shows predicted non-dimensionalized surface pressure contours on the cowl-flap and sidewall surfaces. Note the high-pressure region in the corner between the sidewall and cowl flap. The figure also depicts the locations of three stations where thin-film gauges were placed to measure surface heating.

Comparisons between predicted and measured heating on the cowl flap surface at various x-stations are shown in figures 11-13. Since the vehicle configuration has the boundary-layer trips, the data shown in the figures are those obtained with the trips. The engineering database estimates are also included in figures 11-13 for comparison.

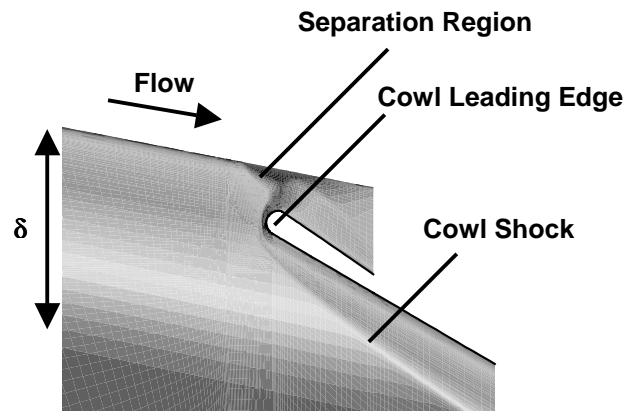


Figure 9. Symmetry-plane flow structure at Mach 10 freestream conditions.

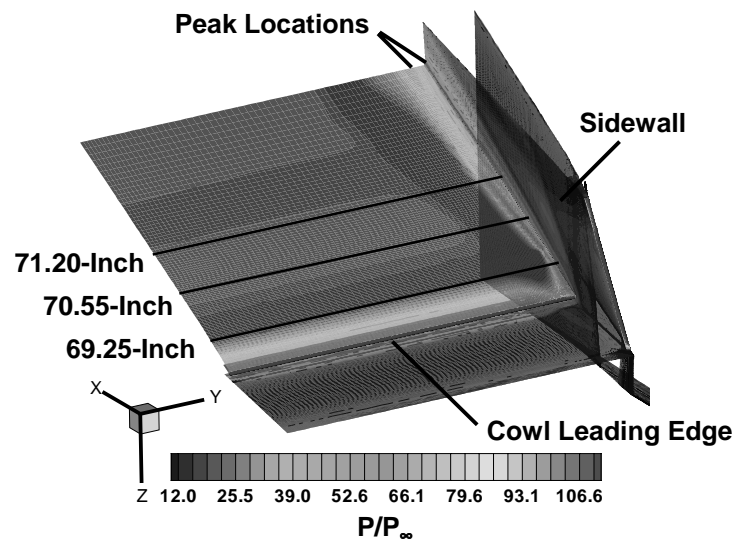


Figure 10. Non-dimensionalized surface pressure contours at Mach 10 with surface instrumentation locations.

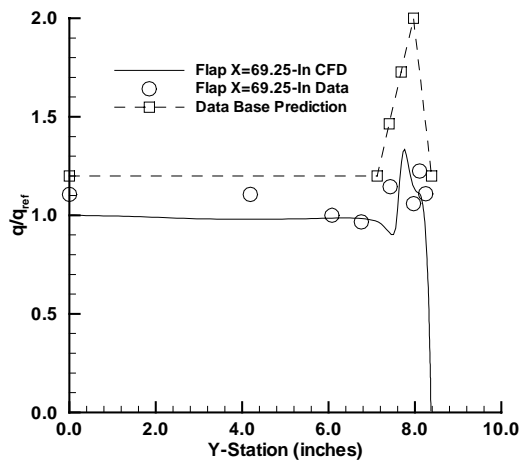


Figure 11. Comparison of Mach 10 predicted and measured heating amplification rates at X=69.25-Inch station.

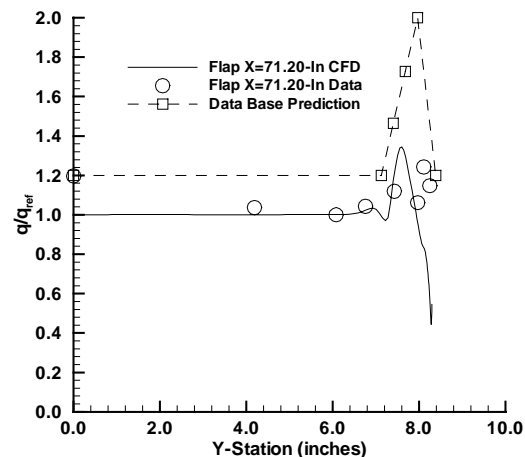


Figure 13. Comparison of Mach 10 predicted and measured heating amplification rates at X=71.2-Inch station.

Additionally, flow spillage around the sides of the plate may cause expansion waves which would influence the flow field in the vicinity of the cowl leading edge. This effect is not expected for the Mach 10 vehicle at the flight condition. Therefore, the measurements are non-dimensionalized by the value at the off-center-line gauge located approximately 6-inches from the center line, which best represents the undisturbed reference value to quantify the localized corner flow effects.

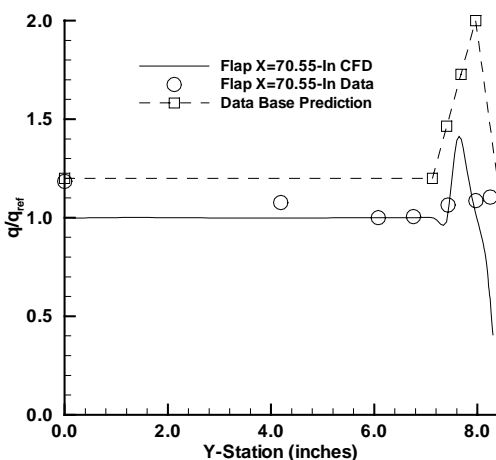


Figure 12. Comparison of Mach 10 predicted and measured heating amplification rates at X=70.55-Inch station.

For consistency, the CFD-predicted values shown in figures 11-13 are non-dimensionalized by the center-line value at each station. The measurements indicate that there is some lateral variation of surface heat fluxes from the center-line to the off-center-line values independent of the influence of corner flow effects. This lateral variation may be the result of spatial variations in test-section conditions and the three-dimensional flow-field effects not modeled in the 2-D forebody-plate calculation.

The CFD predictions and measured peak heating values are similar, with peak amplification rates of 1.3 to 1.4 at each station. Note that the experimental data at the x=70.55-inch station do not indicate similar peak values as the other two stations because of a malfunctioning gauge (at the expected peak heating location). The experimental data indicate that the peak heating location is closer to the corner than predicted by the CFD predictions, which utilized a fully turbulent boundary layer along the inboard sidewall surface. This may suggest that the boundary layer is either laminar or transitional.

The engineering database estimates assumed an amplification rate of 2.0 times the undisturbed turbulent center-line heating rate. Note that this includes the 20-percent factor applied to account for trip-induced vortex interactions. Based on the LENS-derived experimental data and corresponding CFD

predictions, this assumption appears to be conservative.

Figure 14 shows predicted surface heating amplification, progressing along the sidewall surface, at the same x-stations. The heating rates are non-dimensionalized by an undisturbed value just downstream of the sidewall leading edge, so that direct comparisons between the three locations are obtainable. The peak heating for the sidewall occurs near the corner and results from the shock generated by the cowl flap sweeping across the sidewall surface. Available measurements, non-dimensionalized by an experimental value taken near the sidewall leading edge, indicate amplification rates of 4.6, 7.2 and 8.6, respectively at the corresponding stations. Based on inspection of the instrumentation locations, it is likely that the placement of gauges on the sidewall surface did not fully quantify the locus of expected maximum heating locations. The gauge placement locations on the sidewall surface were based on heating enhancement locations predicted by the engineering analysis. The freestream Mach number in the ground tests (Mach 10.7) resulted in shallower shock angles, and therefore, a discrepancy in the peak heating locations.

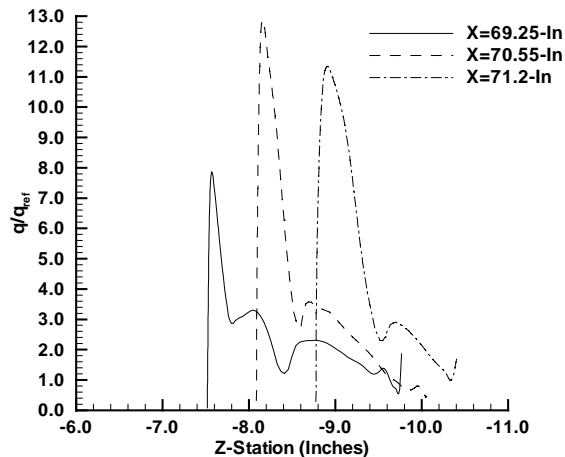


Figure 14. Predicted sidewall surface heating at Mach 10.

The engineering database estimates for sidewall heating amplification rates were referenced to an undisturbed laminar flat plate value. The engineering estimates indicated a peak amplification factor of 15 times the undisturbed laminar value. The Mach 10 calculation, however, assumed a fully turbulent boundary layer on the sidewall surface. In order to make a consistent comparison between the fully turbulent 3-D CFD predictions and the experimental database estimates based on laminar reference values, the effects of the boundary-layer assumption on the amplification factor need to be examined. Figure 15 shows a comparison of 2-D forebody plate calculations with fully laminar and fully turbulent boundary-layer assumptions. These data indicate that a factor of 2 to 2.5 is a conservative estimate to account for heating augmentation for turbulent flow effects. Note that this estimate is also consistent with the data comparison shown in figure 8. This analysis suggests that a factor of 20 or higher over the undisturbed laminar heating rate is possible on the sidewall surface.

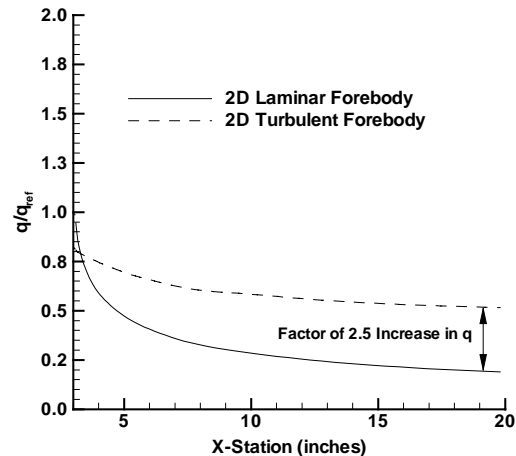


Figure 15. Comparison of surface heating for 2-D forebody laminar and turbulent solutions at Mach 10.

Mach 7 Condition

Presented subsequently are the Mach 7 CFD results, which are compared to the amplification rates estimated in the engineering analysis. Also presented, are some characteristics of the forebody flow-field solution that address the initialization process for the 3-D elliptic cowl-flap/sidewall region. Figure 16

shows forebody streamline traces. The forebody flow-field predictions indicate that at the negative angle-of-attack condition, flow along the forebody surface tends to spill over the chine surfaces. This flow pattern results in a thickening of the chine boundary layer, as detailed in figure 17, which shows Mach number contours at the outflow plane of the forebody. At a position just upstream of the sidewall leading edge, a tendency for streamwise boundary-layer separation along the chine surfaces is observed. This necessitated adjusting the CFD grid interface of the forebody region and the elliptic corner region further upstream to resolve this flow-field feature.

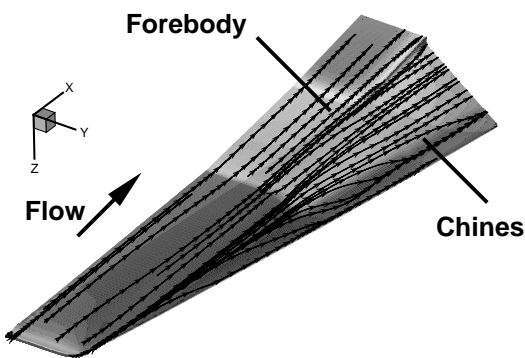


Figure 16. Predicted forebody surface streamtraces at Mach 7.

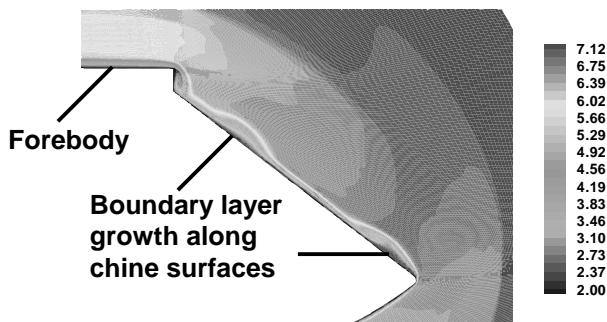


Figure 17. Mach number contours at last station of Mach 7 Forebody marching solution.

Figure 18 shows non-dimensionalized surface pressure contours on the cowl flap and sidewall surfaces. There is a region of high pressure on both the cowl flap and the internal corner region on the sidewall. These high-pressure regions correspond to localized peak-heating regions of these surfaces. Similar pressure contour patterns are evident in the corner region previously shown in figure 10.

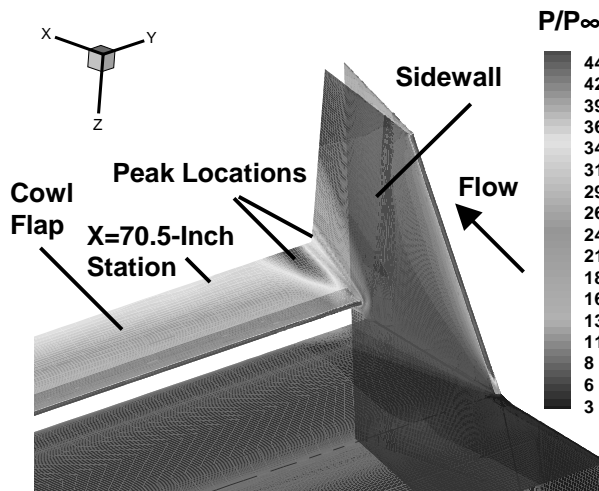


Figure 18. Non-dimensionalized surface pressure contours at Mach 7 flight conditions.

Figures 19 and 20 present plots of non-dimensionalized heating predictions along the cowl flap and sidewall surfaces, respectively, at the outflow plane of the elliptic region ($x=70.5$ -inch station). The predicted heating on the cowl flap surface is non-dimensionalized by the center-line value at this station. The sidewall predictions are non-dimensionalized by a heat flux value near the sidewall leading edge, which represents an undisturbed heating value. This is the same methodology used to examine the Mach 10 sidewall CFD predictions. Heating predictions show an amplification rate of approximately 1.8 referenced to the undisturbed turbulent level at the symmetry plane on the cowl flap surface. An amplification rate of approximately 11.0 referenced to the undisturbed turbulent leading edge value is predicted on the sidewall surface.

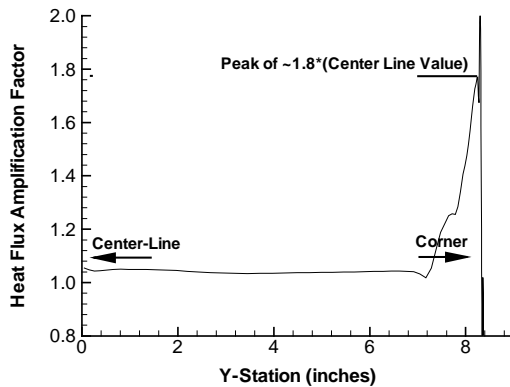


Figure 19. Surface heat flux amplification rates on cowl flap (x=70.5-inch station) at Mach 7.

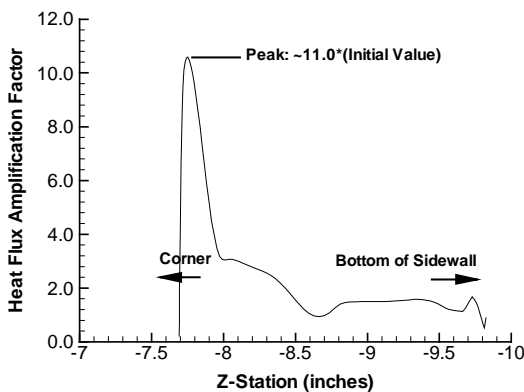


Figure 20. Surface heat flux amplification rates on sidewall (x=70.5-inch station) at Mach 7.

These predicted amplification rates are consistent with the engineering estimates, which were based on existing experimental databases. The engineering analysis predicts a maximum heating amplification factor of 2.0 times the undisturbed turbulent heat flux value on the cowl flap surface near the corner and a maximum amplification factor of 15 times the undisturbed laminar heating value on the sidewall surface resulting from shock impingement. Additionally, the Mach 7 CFD flight solution provides a qualitative assessment of pertinent flow-field features and regions of localized heating at this condition; however, a more comprehensive quantitative analysis of surface heating requires an in-depth modeling of the appropriate flight wall temperatures.

The cowl-flap material survivability issue, at Mach 7 flight conditions, was further addressed experimentally during an extensive test program of the Hyper-X Flight Engine (HXFE) in the NASA-Langley 8-Foot High Temperature Tunnel (HTT)¹⁰. During this experiment, a limiting-case run, performed with the cowl-closed configuration, was obtained using the maximum duration of Mach 7 flow conditions for the facility (approximately 20-25 seconds). This run simulated the maximum integral surface heating exposure during flight. The cowl was successfully actuated upon completion of the run.

Computational Accuracy Assessment

Two issues are addressed as a measure of numerical accuracy of the computational predictions presented herein. The first concerns the iteration convergence criteria and the second concerns an assessment of grid quality to ensure adequate boundary-layer and surface heating resolution.

Iteration convergence of the CFD elliptic regions of the Mach 7 and Mach 10 solutions was deemed adequate by examining integrated surface heat loads and heat flux predictions on the cowl flap and sidewall surfaces. For the Mach 10 calculation, the elliptic corner-flow region was run for 16500 iterations. The integrated heat load on the inboard sidewall surface converged to a less than 1-percent difference between successive runs of 500 iterations and to within 3-percent on the cowl-flap surface. Additionally, the predicted sidewall heat-flux values, center-line heat flux values and amplification rates converged to within 1-percent in most locations between successive runs. The Mach 7 elliptic corner-flow calculation converged to within less than 1-percent on the cowl-flap and sidewall integrated heat flux in 5000 iterations. CFD marching regions were assumed converged after achieving a 5-orders-of-magnitude reduction in the L2-norm of the residual vector at each space-marching plane. Previous experience has shown this to be an adequate convergence criterion for static pressure and skin friction quantities.

Detailed grid convergence studies were not conducted for this specific application because of computational resource requirements to solve the 3-D fully elliptic

calculations. However, a common measure of grid quality near the wall is the grid spacing parameter y^+ , which is defined as:

$$y^+ = \frac{\sqrt{\rho_w \tau_w} \Delta y}{\mu}, \quad (1)$$

where,

ρ_w is the local density near the wall, τ_w is the local-wall shear stress, Δy is the distance from the surface to the cell center of the wall-adjacent control volume and μ is the viscosity coefficient. In reference 11, Dilley commented on grid-spacing requirements to adequately resolve surface heat transfer predictions. This analysis indicated that y^+ values on the order of 2 are necessary to ensure adequate resolution of the boundary layer. Comparisons of flat-plate calculations performed with various grid spacing indicated that for cold-wall boundary conditions, a y^+ value of 1.5 resulted in approximately a 5-percent difference in predicted Stanton number values compared to predictions obtained with a y^+ value of 0.1. The cold-wall boundary condition was shown to be less sensitive to grid spacing than the hot-wall boundary condition.

These highly restrictive grid spacing requirements are not practical for hypersonic vehicle design applications where large volume grids are required to simultaneously resolve geometry and flow-field features. Also, y^+ values must be examined after the solution is obtained, which necessitates multiple solutions to optimize the mesh and to properly assess accuracy based on off-surface grid spacing. An examination of y^+ values for the Mach 10 solution yields values on the order of 2 are present near the inboard sidewall surface, although values on the order of 10 are observed in regions where peak heating amplification rates are predicted. Similar values were observed for the Mach 7 calculation, although reference 11 suggests a more restrictive near-wall grid spacing requirement because of the higher wall temperatures at the flight condition. The Mach 7 predictions are only used to examine relative amplification rates, and therefore, they are sufficient to obtain a qualitative assessment of peak heating locations and flow-field patterns.

Concluding Remarks

An analysis was conducted to determine aerothermodynamic loads on the Mach 7 and Mach 10 X-43 Hyper-X cowl-closed configurations. Documented laminar and turbulent heating data were used to estimate localized heat flux amplification rates on the closed-cowl flap and sidewall surfaces in an engineering-level analysis of surface heating rates. This analysis was used to account for three-dimensional flow-field effects, including trip-induced vortex boundary-layer interactions, corner flow effects and shock boundary-layer interaction effects. Subsequently, thin-film gauge surface heating measurements were obtained at nominal Mach 10 flight total enthalpy conditions for the Mach 10 X-43 cowl-closed configurations. Additionally, CFD predictions were obtained at the same test conditions to examine flow-field structures and provide comparisons with the engineering database predictions and experimental data. The Mach 10 predictions compared favorably with test data and generally predicted similar heating amplification rates on the cowl flap surface compared to the engineering estimates. The thin-film gauges were not placed in a manner to completely capture peak heating rates on the sidewall surface at the Mach 10 experimental conditions, although the CFD predictions indicate that higher localized peak heating are possible compared to the engineering estimates. Lastly, the Mach 7 CFD predictions of peak heating on the cowl-flap and sidewall surfaces are being used in Hyper-X design activities.

Acknowledgements

Scott Berry, Robert Nowak and Christopher Glass in the LaRC Aerothermodynamics Branch contributed to the development of the engineering heating estimates. The Mach 10 experiments were directed by Michael Holden at CUBRC. Chris Glass, Vince Cuda and Wayne Guy at NASA-Langley provided technical review of the paper.

References

1. Freeman, Delma C.; Reubush, David E.; McClinton, Charles R.; Rausch, Vincent L. and Crawford, J. Larry. The NASA Hyper-X Program, Presented at the 48th International Astronautical Conference, October 1997.

2. Settles, G.S. and Dodson, L.J. Hypersonic Shock/ Boundary-Layer Interaction Database, NASA Contractor Report 177577, April 1991.
3. Hackett, C.M. Aerothermodynamic Heating Due to Shock Wave/Laminary Boundary-Layer Interactions in High-Enthalpy Hypersonic Flow. AIAA 93-3135, July 1993.
4. Berry, Scott A.; DiFulvio, Michael, Kowalkowski, Matthew K. Forced Boundary-Layer Transition on X-43 (Hyper-X) in NASA LaRC 20-Inch Mach 6 Air Tunnel. NASA TM-2000-210316, August 2000.
5. Holden, Michael S. Large Energy National Shock Tunnel (LENS), Description and Capabilities. NASA Technical Report AD-A338839, December 1990.
6. White, J.A. and Morrison, J.H. A Pseudo-Temporal Multi-Grid Relaxation Scheme for the Parabolized Navier-Stokes Equations. AIAA 99-3360, June 1999.
7. Wilcox, D.W. Turbulence Modeling for CFD, DCW Industries, La Canada, California, 1998, pp. 119-122.
8. Cockrell, Charles E. Jr.; Englund, Walter C.; Bittner, Robert D.; Dilley, Arthur D.; Jentink, Tom N. and Frendi, Abdelkader. Integrated Aero-Propulsive CFD Methodology for the Hyper-X Flight Experiment. AIAA 2000-4010, Presented at AIAA 18th Applied Aerodynamics Conference, August 2000.
9. Berry, Scott A., Auslender, Aaron H. and Dilley, Arthur D. Hypersonic Boundary Layer Trip Development for Hyper-X. AIAA 2000-4012, August 2000.
10. Huebner, Lawrence D.; Rock, Kenneth E.; Witte, David W.; Ruf, Edward G. and Andrews, Earl H. Jr. Hyper-X Engine Testing in the NASA Langley 8-Foot High Temperature Tunnel. AIAA 2000-3605, Presented at the AIAA/ASME/SAE/ASEE 36th Joint Propulsion Conference, July 2000.
11. Dilley, Arthur D. Evaluation of CFD Turbulent Heating Prediction Techniques and Comparison with Hypersonic

Experimental Data. NASA Contractor Report CR-2001-210837, March 2001.